Proceedings of the ASME 2010 International Design Engineering Technical Conferences & Computers and Information in Engineering Conference
IDETC/CIE 2010
August 15-18, 2010, Montreal, Quebec, Canada

DETC2010-28878

DEVELOPING A KINEMATIC ESTIMATION MODEL FOR A CLIMBING MOBILE ROBOTIC WELDING SYSTEM

Aaron T. O'Toole, Stephen L. Canfield
Tennessee Technological University
Dept. of Mechanical Engineering
Cookeville, Tennessee, 38505
United States of America
Aotoole21@tntech.edu; SCanfield@tntech.edu

Abstract:
Skid steer tracked-based robots are popular due to their mechanical simplicity, zero-turning radius and greater traction. This architecture also has several advantages when employed by mobile platforms designed to climb and navigate ferrous surfaces, such as increased magnet density and low profile (center of gravity). However, creating a kinematic model for localization and motion control of this architecture is complicated due to the fact that tracks necessarily slip and do not roll. Such a model could be based on a heuristic representation, an experimentally-based characterization or a probabilistic form. This paper will extend an experimentally-based kinematic equivalence model to a climbing, track-based robot platform. The model will be adapted to account for the unique mobility characteristics associated with climbing. The accuracy of the model will be evaluated in several representative tasks. Application of this model to a climbing mobile robotic welding system (MRWS) is presented.

1. Introduction:

Skid steer tracked-based robots are recently becoming more popular due to their mechanical simplicity, zero-turning radius and improved traction. These features are equally important when employed on particular types of mobile robot platforms designed for climbing. As an example, [11] demonstrates a permanent magnet-based climbing platform to automate inspection tasks in power plants. In a case such as this, tracks offer unique benefits for suspension design and the ability to have a large density of magnets contacting the climbing surface. One limitation of skid-steer vehicles is the fact that they reflect poor power efficiencies when turning; this is because they don't resemble the pure rolling constraint that is applicable to wheeled vehicles. Also, the problems of localization and motion control for skid-steer robots is extremely difficult since the assumptions of no-slip/pure rolling do not apply as they do with traditional wheeled robots. This is true in the traditional sense (where gravity provides the stabilizing forces) or in the application to a climbing mobile robot.

In the traditional applications of skid-steer mobile robots, much research has been focused on creating improved models to describe the motion of the mobile platform. Some of this research has created models that predict the amount of slip through symbolic representations of the interaction between the tracks (or wheels) and ground [1-3]. Alternatively, a larger emphasis has focused on developing kinematic models that rely on an empirically-derived set of parameters (we will call these kinematic characteristic parameters) [4-9]. The result is a linear model of the same form as an idealized differential steer system that minimizes pose errors in the sense of dead reckoning under a particular set of operating conditions. The latter approach is most commonly achieved by estimating the kinematic equivalence parameters through comparing internal encoder data on wheel/track motion to external vehicle pose data, which can be obtained from such sensors as encoder trailers [10], G.P.S. [5], inertial measurement units [4,6,7], laser scanners [8], or cameras [9]. Mandow et al. have gone as far as realize a geometric interpretation of the slip correction factors based on the geometric analogy with an ideal differential drive model [5]. Once the pertinent kinematic information is gathered, it is possible to determine the kinematic equivalent parameters through optimization to minimize a suitable kinematic objective. This method usually includes some form of state estimator based on simultaneous localization and slip estimations in order to produce more reliable localization estimates. Examples of such state estimators are: a Fast Kalman Filter (FKF) that fuses information from an experimentally derived kinematic model and sensor data from an onboard inertial measurement system [4], an Extended Kalman Filter (EKF) which incorporates vehicle velocity constraints and estimations in addition to wheel slip approximations in order to reduce drift errors associated with the integration of inertial measurements [6,7], and a Sliding

Mode Observer (SMO) used to approximate slip parameters to facilitate a reduction in velocity measurement errors generated by optical flow-based motion estimation [9].

While the method of utilizing an empirically-derived kinematic model is by no means perfect, it is a great improvement when compared to using the kinematic model of a non-holonomic wheeled vehicle for a tracked vehicle. It is noted that the method of characterizing kinematic parameters is only valid for robots traveling at relatively low speeds since it neglects centrifugal dynamics, and assumes slippage only occurs due to steering. Nevertheless, it is still an attractive approach for some applications, such as, robotic welding, remote ultrasonic inspection, etc. of which the end effector/tool requires low speeds. Past research of this type has proven satisfactory for ground based vehicles; however, the authors are unaware of any research regarding this procedure with climbing mobile robots.

In this paper we propose to develop an improved kinematic model for a mobile climbing robotic platform. This climbing robot relies on skid steering for surface navigation, but employs a track system with discrete contact elements and magnetic forces (rather than gravity) to maintain equilibrium during locomotion. The model will be adapted to account for the unique mobility characteristics associated with climbing. The accuracy of the model will be evaluated in several representative tasks. Application of this model to a climbing mobile robotic welding system (MRWS), shown in Fig. 1, is presented.

2. OVERVIEW of MRWS:

The MRWS consists of a permanent magnetic, track-based mobile robot weighing approximately 30 kilograms. The tracks consist of a series of permanent magnet feet mounted on a driving chain, supported by two sprockets (one driven), tensioning mechanism and suspension mechanism. The robot can climb any ferrous (steel) structure in any orientation; vertical, horizontal, even upside down and is capable of climbing surfaces with a moderate amount of surface variation dependent on the degree of travel in the track suspension and chassis degree of freedom. The platform has a payload of approximately 45 kg, which consists primarily of a commercial wire feeder, welding torch, torch manipulator and sensor package. The torch manipulator is independently suspended to isolate it from any motion disturbances from the robot platform and has 4 degrees-of-freedom to provide local control to the torch. The torch travel angle (pitch), work angle (roll), and torch depth are adjusted manually, while the torch translation is actuated with a brushless D.C. motor. Coordinated control of the robot platform motion and torch manipulator is provided by the onboard processor and control algorithm, allowing the MRWS to produce a variety of desired weld patterns in a semi-autonomous fashion. Figure 1 shows a field ready version of the MRWS with the major components highlighted, and Fig. 2 shows the MRWS conducting a weld.

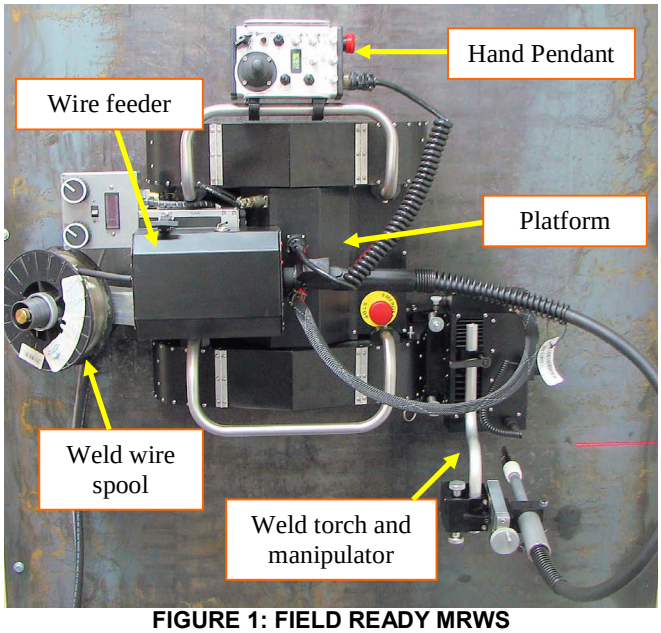

FIGURE 1: FIELD READY MRWS

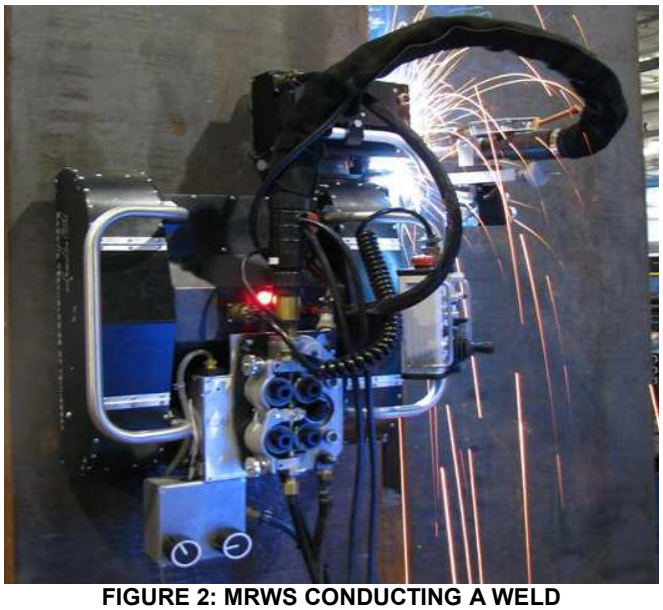

FIGURE 2: MRWS CONDUCTING A WELD

Early MRWS prototypes achieved lateral torch positioning solely from the torch manipulator, while the platform itself traveled a straight line. In order to prevent the weld groove position from exceeding the reach of the torch manipulator, the operator was occasionally required to make small adjustments to the platform's trajectory via a hand pendant. The kinematic model presented in this paper is the basis for a control scheme that will allow this maneuver to be preformed autonomously without changing the pose of the torch with respect to the work piece. In doing so, the MRWS will effectively guarantee the weld groove remains in the workspace of the torch manipulator, enabling the operator to focus more on the welding process without concerning the boundary limits of the workspace of the torch manipulator. Not shown in Fig. 1 is a vision-based seam tracking system that will provide the MRWS adequate weld groove position information required to implement the closed loop controller, which will not be discussed in this paper.

3. Model:

In developing a kinematic model for the MRWS, several assumptions are made: 1) rigid chassis, 2) rigid, straight track suspension, 3) constant velocity relationship between the drive motors and corresponding track velocity, 4) planar climbing surface with uniform frictional properties.

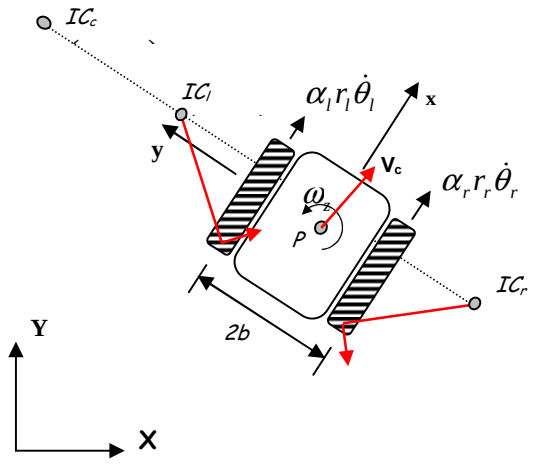

FIGURE 3: MRWS MODEL SCHEMATIC

The kinematic model is based on the schematic presented in Fig. 3. A local frame {R} with coordinates {*x*,*y*,*z*} is attached to the geometric center of the robot platform at point *P* as shown in Fig. 3, with the *z* axis normal to the climbing surface, the *x* axis centered and parallel to the tracks and the *y* axis completing the right-hand frame. Frame {I} with coordinates {*X*,*Y*,*Z*} represents the inertia frame. The forward kinematics relate the input parameters to robot pose on the planar climbing surface as,

$$\left[V_x, V_y, \omega_z\right]_R^T = \mathbf{f}\left(\dot{\theta}_r, \dot{\theta}_l\right) \tag{1}$$

Where V_x and V_y are the robot's linear velocities in the *x* and *y* direction respectively, ω_z is the angular velocity of the robot, and $\dot{\theta}_r, \dot{\theta}_l$ are the angular velocities of the right and left drive motors. The, robot velocity can be projected to the global frame through a *z*-axis rotation,

$$\left[V_X, V_Y, \omega_Z\right]_I^T = \mathbf{R}_I^R \left[V_x, V_y, \omega_z\right]_R^T \tag{2}$$

Following the method proposed in part by [5], the kinematic function **f** in (1) will be composed as an (optimal) linear approximation in the form,

$$\left[V_x, V_y, \omega_z\right]^T = \mathbf{K}_{eq} \begin{bmatrix} \dot{\theta}_r \\ \dot{\theta}_l \end{bmatrix} \tag{3}$$

where $\mathbf{K}_{eq}$ is a 3x2 kinematic equivalence matrix that approximates the kinematic behavior as a linear function of the inputs and a set of six constant coefficients that may be experimentally determined to best characterize the mobile platform. Following the method presented in [5], these coefficients will be defined based on geometric locations of the Instant Centers of Rotation (IC) associated with the robot chassis (IC_c) and the left and right tracks (IC_l, IC_r), as well as two unit-less kinematic correction factors for the left and right tracks (α_l, α_r). These parameters will be called kinematic equivalence parameters and are shown on the schematic in Fig. 3. The instantaneous center of rotation for the robot chassis (IC_c) is located in the robot frame with coordinates (x_c,y_c) while the instant centers for the left and right tracks (IC_l, IC_r) are located in {R} with coordinates (x_l, y_l) and (x_r, y_r) respectively. According to the Arnhold-Kennedy theorem which states that the three instantaneous centers of rotation shared by three rigid bodies in relative motion to one another all lie on the same line, and the fact that the angular velocity of the chassis is the same as that of the two tracks, it is known that IC_r IC_l and IC_c all lie on the same line which is parallel to the *y* axis. This allows the instant center coordinates and platform translational and rotational velocities to be written as,

$$y_c = \frac{V_x}{\omega_z} \tag{4}$$

$$x_c = x_l = x_r = \frac{V_y}{\omega_z} \tag{5}$$

$$y_l = \frac{-\alpha_l r_l \dot{\theta}_l + V_x}{\omega_z} \tag{6}$$

$$y_r = \frac{-\alpha_r r_r \dot{\theta}_r + V_x}{\omega_z} \tag{7}$$

where α_l, α_r are the kinematic correction factors associated with the left and right tracks to account for inaccuracies in the gear ratio calculation, i.e. mechanical wear, belt tension, etc. and r_l, r_r are the ideal constant ratios relating linear track velocity to input actuator rotation for the left and right sides respectively. Rewriting equations (4)-(7) in the form of (3) yield the kinematic equivalence matrix,

$$\mathbf{K}_{eq} = \frac{1}{\left(y_r - y_l\right)} \begin{bmatrix} y_r \alpha_l r_l & -y_l \alpha_r r_r \\ x_c \alpha_l r_l & -x_c \alpha_r r_r \\ \alpha_l r_l & -\alpha_r r_r \end{bmatrix} \tag{8}$$

As defined here, the kinematic equivalence matrix is described using five unique kinematic characteristic parameters, three instantaneous centers of rotation coordinates (x_c, y_l, y_r) and two transmission correction coefficients (α_l, α_r), and two fixed gear ratio parameters (r_l, r_r). The two gear ratios are defined at the design level, while the remaining five parameters depend on both robot design and operating conditions. Boundedness of the kinematic equivalence matrix (8) is necessary for subsequent use and depends on the bounded nature of the kinematic relationships in (5) – (7) (note that equation (4) is not bounded). As noted in [5, 7, 8], (5)-(7) remain bounded as the vehicle approaches straight-line motion and kinematic motion is preserved and therefore are generally

applied to systems in which dynamic effects may be reasonably neglected and external forces are negligible. In the proposed use, applying the kinematic equivalence to describe the motion of a climbing robot which experiences gravitational forces directly in the *x*-*y* plane, requires further consideration before direct application of (8), (3).

3.1 Verification of Bounded Nature of the Kinematic Model:

As noted above, the robot's instant center position in the *y* direction approaches an infinite value during straight line motion as is evident in (4) as ω_z goes to zero. However, under the kinematic relationships described in (5)-(7), the track instant center locations (x_c , y_l , y_r), remain bounded since the numerators and denominators approach infinitesimals of the same order during straight line motion [5]. External forces or dynamic effects that induce slippage (other than that required for steering) would violate these kinematic relationships and must be considered before application of (8) and (3). While dynamic effects may be reasonably ignored in MRWS operation, gravitational effects are significant while climbing and may produce slipping. Following the method presented by Kozlowski [3] in which stability is defined under significant centrifugal dynamics, requirements on MRWS design and operation will be constructed.

The dynamic equation of motion for the MRWS can be written in the global frame as:

$$\mathbf{M(q)\ddot{q} + F(\dot{q}) + G(q) = E(q)\tau} \tag{9}$$

Where $\mathbf{q} = \{X, Y, \theta\}^T$ represents the robot pose in the global frame, $\mathbf{M} = \text{diag}\{m, m, I\}$ is the inertia matrix with m and I denoting the mass and inertia of the MRWS platform, $\boldsymbol{\tau} = \{\tau_l, \tau_r\}^T$ is the input torques vector, **F** is a vector containing resisting forces and torques involved with track/ground interaction, **E** is a 3x2 input transformation matrix, and **G** is the gravitational force vector. Note that equation (9) is written in the inertial frame {*X*, *Y*, *Z*}, where *X* and *Y* are in the plane of the climbing surface, and *Z* is orthogonal to the surface. This model is more useful when considered in the local frame. Using the mapping given in (2), consider the following,

$$\bar{\mathbf{M}}\dot{\mathbf{r}} + \bar{\mathbf{C}}\mathbf{r} + \bar{\mathbf{F}} + \bar{\mathbf{G}} = \bar{\mathbf{E}}\boldsymbol{\tau} \tag{10}$$

Where, $\mathbf{r} = \{V_x, V_y, \omega_z\}^T$ represents the robot velocities in the local frame, $\bar{\mathbf{M}} = \mathbf{M}$, $\bar{\mathbf{G}} = \{mg'\sin(\theta), mg'\cos(\theta), 0\}^T$, θ the rotation from local to global frame, *g*' the gravity component in the climbing plane, vector $\bar{\mathbf{F}} = \{F_{tx}, F_{ty}, M_t\}^T$, with F_{tx} F_{ty} and M_t denoting the forces and torques causes by the track/surface interaction respectively, and the input transformation matrix $\bar{\mathbf{E}}$ and the matrix containing the centripetal and coriolis terms $\bar{\mathbf{C}}$ are as follows,

$$\bar{\mathbf{E}} = \frac{1}{r}\begin{bmatrix} 1 & 1 \\ 0 & 0 \\ -b & b \end{bmatrix}; \bar{C} = \begin{bmatrix} 0 & -m\omega_z & 0 \\ m\omega_z & 0 & 0 \\ 0 & 0 & 0 \end{bmatrix}. \tag{11}$$

Expanding (10), and isolating $\dot{V}_y$ yields:

$$\dot{V}_y = -\omega_z V_x - \frac{F_{ty}}{m} - g'\cos(\theta) \tag{12}$$

Since the torque vectors do not directly contribute to the lateral velocity (velocity in the local *y* axis), its motion is not controllable. We will assume this term remains small and is negligible. To be bounded, the resisting forces F_{ty} must be sufficient to cancel the dynamic effects ($\omega_z V_x$) and gravitational component ($g'\cos(\theta)$). In order to do so, information about the track/surface interaction forces in the lateral direction are needed, which are extremely difficult to obtain, but in this paper they will be simplified to the following model:

$$F_{ty} = \left(\sum_{i=1}^{n} -\mu N_i \angle v_i\right) \cdot \hat{y} \tag{13}$$

Where v_i is velocity vector of foot *i*, and in the case of the MRWS covered in this paper μ is the kinetic coefficient of friction for steel on steel ($\mu \approx 0.8$), *n* is the number of magnets in contact with the surface at any given time ($n = 16$). *N* is the normal force between the magnet and surface, which when the MRWS is climbing a vertical surface can be estimated as simply the magnetic force supplied by one foot, assuming the platform has a low center of gravity and the feet are uniformly loaded ($N = 125$ N).

Note that F_{ty} in (13) increases when all the magnets' lateral velocities (in the *y* direction) are in the same direction, which is the case when $x_c \notin \{-L/2, L/2\}$, as shown in Fig. 4.

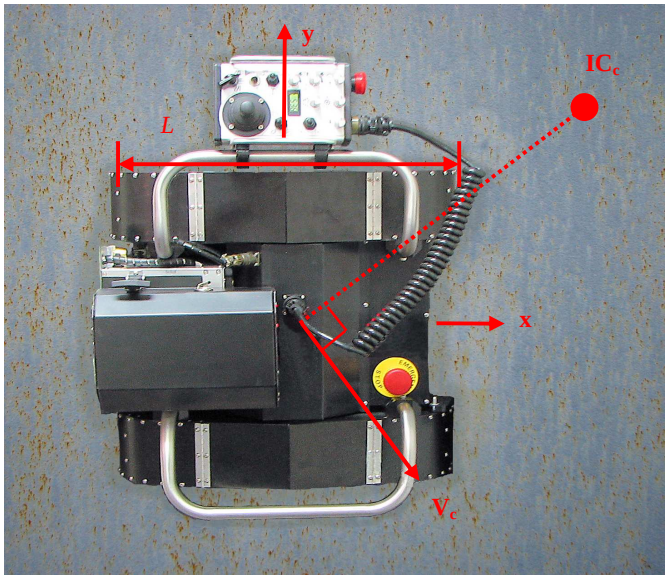

FIGURE 4: IC_c OUTSIDE PERMITTED RANGE

If a limit were applied to the $\omega_z V_x$ term in (12) to insure that

$$F_{ty} < -\frac{x_c}{\sqrt{x_c^2 + y_c^2}} \sum_{i=1}^{n} \mu N_i \,, \qquad (14)$$

the condition for bounded motion could be written as,

$$\left|\omega_z V_x\right| < -\frac{x_c}{\sqrt{x_c^2 + y_c^2}} \frac{1}{m} \sum_{i=1}^{n} \mu N_i - g' \left|\cos(\theta)\right| \qquad (15)$$

And this will effectively guarantee:

$$x_c \in \{-L/2, L/2\} \qquad (16)$$

(note that the bounded condition is given at the limits of this region).

Now that the conditions of boundedness have been described, the kinematic equivalence matrix can be evaluated for application to the MRWS. The two gear parameters in (8) evolve directly from the platform design while the remaining five kinematic characteristic parameters will be identified through an experimental process described in the next section and assumed to be constant when characterizing a general class of operational conditions. Once evaluated, the kinematic equivalence matrix can be used in a predictive fashion for robot motion tracking and control based for a given platform.

4. Indentifying the Kinematic Characteristic Parameters:

The kinematic characteristic parameters depend on both robot design and operating conditions. For the purposes of this paper, these parameters will be determined experimentally for specific classes of operational conditions (surface conditions, wall configurations, etc.), and then will be assumed to remain constant during operation in conditions of the particular type. Following similar procedures demonstrated in [5]. The kinematic parameters will be determined as a set that minimizes the objective function based on error in position estimate over a general operational task under a defined set of conditions. This leads to the proposed objective:

$$f(\mathbf{q}) = \sum_{i=1}^{N} \left[\left(\Delta x_i^* - \Delta x_i\right)^2 + \left(\Delta y_i^* - \Delta y_i\right)^2 + \left(\Delta\theta_i^* - \Delta\theta_i\right)^2 \right] \qquad (17)$$

where Δx_i, Δy_i and $\Delta\theta_i$, are the actual pose displacement over motion segment i to $i+1$ and Δx_i^*, Δy_i^* and $\Delta\theta_i^*$, are the pose displacements predicted by the kinematic equivalence matrix, over N+1 state measurements and vector **q** contains the five characteristic parameters. The pose displacements are determined based a first-order Euler integration. For the purposes of this paper, the actual pose displacements are based on estimates of motion from a set of dedicated two-axis wheel encoders mounted on the robot platform. The kinematic characteristic parameter set **q** result as the optimal set to objective function (17) using a nonlinear least-squared search employed in Matlab.

4.1 Evaluation of the actual parameter set:

The actual pose displacements are based on estimates of state derived from two auxiliary encoded trailer wheels mounted on the robot platform. A schematic of this system is shown in Fig. 5. Encoders report the orientation (γ_1, γ_2) and rotation (β_1, β_2) of each wheel. Based on these measurements, estimates (termed actual for the purposes of this paper) of the robot motion are given as:

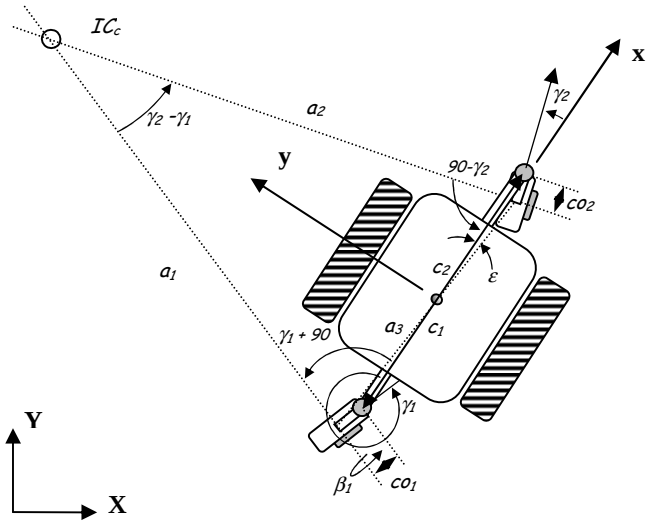

FIGURE 5: SCHEMATIC OF AUXILIARY TRAILER SYSTEM

$$\left[V_x^*, V_y^*, \omega_z^*\right]^T = \mathbf{f}^*\left(\gamma_1, \gamma_2, \dot{\beta}_1\right) \qquad (18)$$

With

$$f_1^*\left(\gamma_1, \gamma_2, \dot{\beta}_1\right) = V_x = \frac{\dot{\beta}_1 r_1 \sin(\gamma_2 - \gamma_1)}{a_3 \cos(\gamma_2 + \varepsilon)} \left(-co_1 \sin(\gamma_1) + \frac{a_3 \cos(\gamma_2 + \varepsilon)\cos(\gamma_1)}{\sin(\gamma_2 - \gamma_1)} \right) \qquad (19)$$

$$f_2^*\left(\gamma_1, \gamma_2, \dot{\beta}_1\right) = V_y = \frac{\dot{\beta}_1 r_1 \sin(\gamma_2 - \gamma_1)}{a_3 \cos(\gamma_2 + \varepsilon)} \left(c_1 + co_1 \cos(\gamma_1) + \frac{a_3 \cos(\gamma_2 + \varepsilon)\sin(\gamma_1)}{\sin(\gamma_2 - \gamma_1)} \right) \qquad (20)$$

$$f_3^*\left(\gamma_1, \gamma_2, \dot{\beta}_1\right) = \omega = \frac{\dot{\beta}_1 r_1 \sin(\gamma_2 - \gamma_1)}{a_3 \cos(\gamma_2 + \varepsilon)} \qquad (21)$$

Where

$$a_3 = \sqrt{(c_{1x} - c_{2x})^2 + (c_{1y} - c_{2y})^2} = \sqrt{(-c_1 - co_1\cos(\gamma_1) - c_2 + co_2\cos(\gamma_2))^2 + (-co_1\sin(\gamma_1) + co_2\sin(\gamma_2))^2} \qquad (22)$$

and

$$\varepsilon = \operatorname{atan2}\left(\left(c_{2y} - c_{1y}\right), \left(c_{2x} - c_{1x}\right)\right)$$
$$= \operatorname{atan2}\left(\left(-co_2 \sin(\gamma_2) + co_1 \sin(\gamma_1)\right), \left(c_2 - co_2 \cos(\gamma_2) + c_1 + co_1 \cos(\gamma_1)\right)\right) \quad (23)$$

The geometric parameters, c_1, c_2, co_1, co_2 are shown in Fig. 5 and c_{1x}, c_{1y}, c_{2x}, c_{2y} are the (x, y) coordinates along c_1, c_2.

4.2 Motion displacement:

The predicted and actual motion displacements can now be determined from the kinematic models given for the MRWS (9), (3) and the auxiliary encoder set (16). These are evaluated numerically using a trapezoidal integration rule. This results in the collection of discrete motion displacements employed in the objective function (15) as,

$$\Delta x_i = \tfrac{1}{2}\left(V_{x,i} + V_{x,i+1}\right)\Delta t \quad (24)$$
$$\Delta y_i = \tfrac{1}{2}\left(V_{y,i} + V_{y,i+1}\right)\Delta t \quad (25)$$
$$\Delta \theta_i = \tfrac{1}{2}\left(\omega_{x,i} + \omega_{x,i+1}\right)\Delta t \quad (26)$$

and

$$\Delta x^*_i = \tfrac{1}{2}\left(V^*_{x,i} + V^*_{x,i+1}\right)\Delta t \quad (27)$$
$$\Delta y^*_i = \tfrac{1}{2}\left(V^*_{y,i} + V^*_{y,i+1}\right)\Delta t \quad (28)$$
$$\Delta \theta^*_i = \tfrac{1}{2}\left(\omega^*_{x,i} + \omega^*_{x,i+1}\right)\Delta t\,. \quad (29)$$

5. Example applications:

A series of example applications are provided next. These examples will consider the MRWS performing manufacturing (welding) in three configurations; flat, in position weld, and horizontal and vertical, out of position weld. The MRMS used in this experiment is 39.4 by 39.4 cm, weighs 18.1 kg, and has a total of 42 permanent magnets, roughly 16 of which are in contact with the surface at all times. The magnets are 6.35x 1.9x .64 cm neodymium iron boron magnets (grade N3520), which give the tracks a combined pull strength of roughly 2000 N. The hardware used for data acquisition consists of five optical encoders (one on each drive shaft, one on the front encoder trailer measuring γ_2, and two on the rear trailer measuring γ_1 and β_1), an eight-channel quadrature encoder counter from Measurement Computing (USB-QUAD08), and a laptop equipped with MATLAB software for data storage.

For each configuration, the MRMS is first driven over a series of maneuvers that both characterize typical tasks in that configuration (welding in straight lines, constant radius curves) and span a typical workspace. While undergoing these task maneuvers, time-based system data is collected to be used in the optimal kinematic identification process (section 3). The resulting set of kinematic equivalence parameters for the flat surface operation are then available to be used to improve pose prediction, control, etc. The results of this process over the three configurations follow. Table I lists the resulting kinematic characteristic parameters for each case and compare these to an idealized differential steer model. Figures 6-8 provide sample demonstration of the kinematic equivalence model in use for each configuration, where an alternative task path (one not directly used in the optimal characterization process above) is traversed with comparisons made between an idealized differential steer model and the optimized kinematic equivalence model. Finally, Table II presents a scalar quality measure for the kinematic equivalence model for each task, shown as the sum squared error in robot pose parameters.

TABLE I: KINEMATIC CHARACTERISTIC PARAMETERS

Orientation/ Parameter	Flat	Horizontal	Vertical	Idealized model
x_c	-5.20	-5.22	-1.90	0
y_l	14.78	-15.92	-20.86	-6.44
y_r	-14.93	15.12	21.98	6.44
α_l	0.98	1.09	1.02	1.0
α_r	0.92	1.03	1.06	1.0

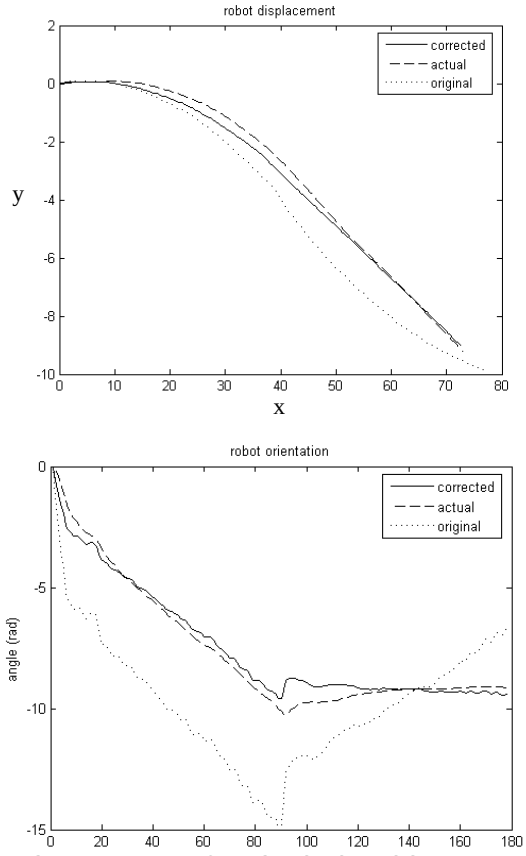

FIGURE 6: PREDICTING ROBOT POSE IN FLAT ORIENTATION (A) POSITION, X, Y (B) ORIENTATION, θ

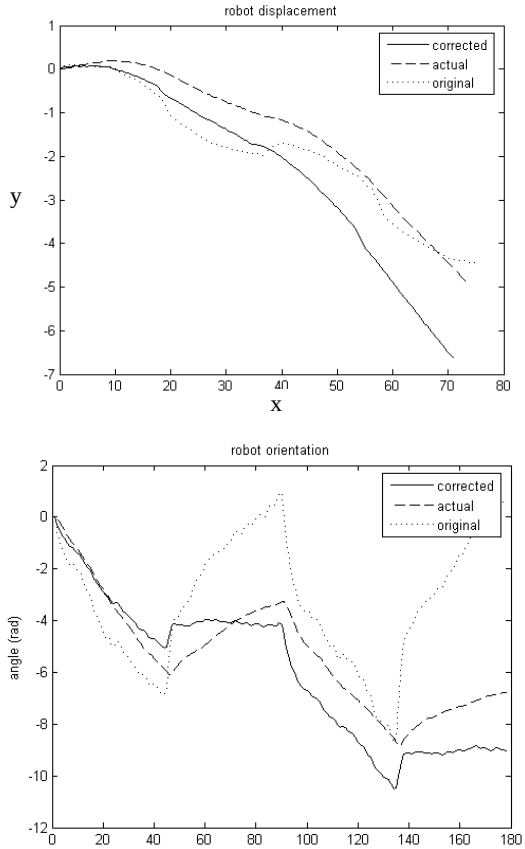

FIGURE 7: PREDICTING ROBOT POSE IN HORIZONTAL ORIENTATION (A) POSITION, X, Y (B) ORIENTATION, θ

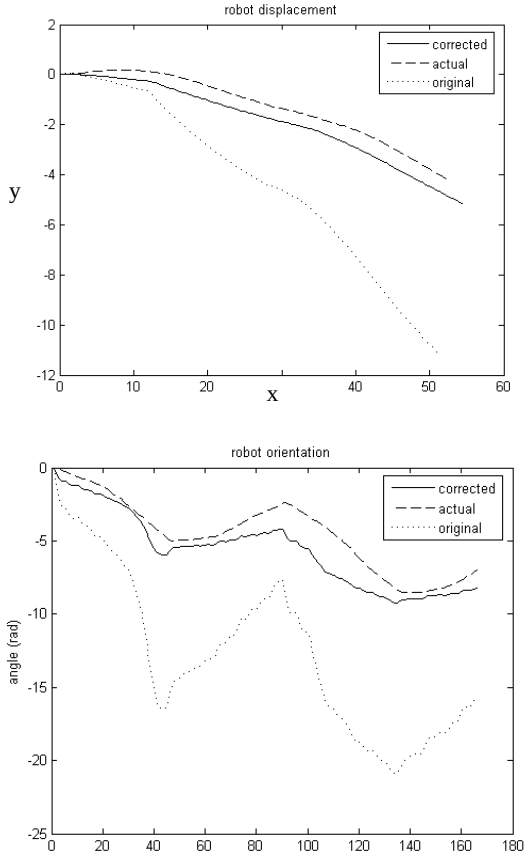

FIGURE 8: PREDICTING ROBOT POSE IN VERTICAL ORIENTATION (A) POSITION, X, Y (B) ORIENTATION, θ

TABLE II: ERROR ASSOCIATED WITH CORRESPONDING MODEL

	Flat orientation (Fig. 6)		Horiz. orientation (Fig. 7)		Vert. orientation (Fig. 8)	
	optimal	idealized	optimal	idealized	optimal	idealized
ΔX^*	0.543	1.504	0.975	1.134	0.638	0.754
ΔY^*	0.133	1.085	0.801	0.533	0.582	2.914
$\Delta \theta^*$	0.314	2.804	1.077	2.579	1.097	8.176
$\Delta_{total}{}^*$	0.989	5.392	2.854	4.246	2.317	11.843

* Square of mean squared error

It should be noted that the tracked platform of the MRWS isn't capable of producing speeds high enough to exceed the inequality in (16), and therefore its behavior remains bounded at all times for these examples. Due to limitations of the experimental platform, the bounded condition proposed is not experimentally tested.

6. Results and Conclusions:

This paper has extended an experimentally-based kinematic equivalence model to a climbing, track-based robot platform. The model is adapted to account for the unique mobility characteristics associated with climbing. The limitations of the model are described as a function of the vehicle design parameters (mass, dimensions, magnetic feet, etc.) and bounds on the product of rotational and translational speed during operation. The process of acquiring the five kinematic characteristic parameters are demonstrated over three distinct categories of operation for the welding robot: welding in position (flat), welding out of position (horizontal) and welding out of position (vertical). Each configuration was evaluated using the same vehicle setup on generally clean, unpainted steel. The resulting parameters are provided in Table I. The kinematic parameters for flat and horizontal operation are similar, while the vertical operation demonstrated a departure in parameters of about 25%. This increase is attributed to the influence of gravity in the primary direction of travel. It should be noted that in all three cases, the kinematic transmission correction factor (α) was very close to one – close to the ideal model. Alternatively, the track instant centers were 2.5 times (or more) greater than the idealized case, indicating a large degree of slippage during any type of steering maneuver. The kinematic equivalence model was then used to predict the position of the robot in operation in all three configurations, using the suggested characteristic parameter set for each corresponding configuration. These results are shown in Fig. 6-8. A comparison of the error relative to an idealized model is shown in Table II. Table II demonstrates a significant reduction in error when predicting robot pose with the kinematic equivalence model. This model will form the basis for kinematic control of welding tasks on the MRWS.

References:

1. Yi, J., Song, D., Zhang, J., and Goodwin, Z., 2007, "Adaptive Trajectory Tracking Control of Skid-Steered Mobile Robots," *IEEE International Conference on Robotics and Automation,* Roma, Italy, 10-14, pp. 2605-2610.

2. Le, A. T., Rye, D. C., and Durrant-Whyte, H. F., 1997, "Estimation of Back-soil Interactions for Autonomous Tracked Vehicles," *IEEE International Conference of Robotics and Automation*, Albuquerque, New Mexico, pp. 1388-1393.
3. Kozlowski, K., and Pazderski, D., "Practical Stabilization of a Skid-steering Mobile Robot – A Kinematic-based Approach," *IEEE 3rd International Conference on Mechatronics*, pp.519-524.
4. Anousaki, G., and Kyriakopoulos, K. J., 2004, "A Dead-Reckoning Scheme for Skid-Steered vehicles in Outdoor Environments," *IEEE International Conference of Robotics and Automation*, New Orleans, LA, pp. 580-585.
5. Mandow, A., Martínez, J. L., Morales, J., Blanco, J. L., García-Cerezo, A., and Gonzàlez, J., 2007, "Experimental kinematics for wheeled skid-steer mobile robots," *IEEE/RSJ International Conference on Intelligent Robots and Systems*, San Diego, CA, USA, pp. 1222-1227.
6. Yi, J., Zhang, J., Song, D., and Jayasuriya, S., 2007, "IMU-based Localization and Slip Estimation for Skid-Steered Mobile Robots," *IEEE/RSJ International Conference on Intelligent Robots and Systems*, San Diego, CA, USA, pp. 2845-2850.
7. Yi, J., Wang, H., Zhang, J., Song, D., Jayasuriya, S., and Liu, J., 2009, "Kinematic Modeling and Analysis of Skid-Steered Mobile Robots with Applications to Low-Cost Inertial-Measurement-Unit-Based Motion Estimation," *IEEE Transactions on Robotics*, v. 25, n. 5, pp. 1087-1097.
8. Martinez, J. L., Mandow, A., Morales, J., Pedraza, S., and Garcia-Cerezo, A., 2005, "Approximating Kinematics for Tracked Mobile Robot," *The International Journal of Robotics Research*, v. 24, n. 10, pp. 867-878.
9. Song, X., Seneviratne, L. D., Althoefer, K., and Song, Z., 2008, " A Robust Slip Estimation Method for Skid-Steered Mobile Robots," *10th International Conference on Control, Automation, Robotics, and Vision*, Hanoi, Vietnam, 17-20, pp. 279-284.
10. Fan, Z., Borenstein, J., Wehe, D., and Koren, Y., 1995, "Experimental Evaluation of an Encoder Trailer for Dead-reckoning in Tracked Mobile Robots," *IEEE International Symposium on Intelligent Control*, Monterey, CA, USA, pp. 571-576.
11. Canfield, S. L., Beard, J. W., Coffey, M. R., and S. M. Halcomb, 2005, "Robotic Inspection in Power Plants, "*ISA 51st Annual Instrumentation Symposium*, Knoxville, TN.